Polymerization-Induced Phase Separation. 2. Morphological Analysis

Philip K. Chan and Alejandro D. Rey*

Department of Chemical Engineering, McGill University, 3480 University, Montreal, Quebec H3A 2A7, Canada

Received July 22, 1996; Revised Manuscript Received November 22, 1996⊗

ABSTRACT: A model composed of the nonlinear Cahn−Hilliard and Flory−Huggins theories for spinodal decomposition (SD) and a second-order rate equation for polymerization for the self-condensation of a trifunctional monomer is used to study the polymerization-induced phase separation (PIPS) phenomena. The numerical results are consistent with experimental observations. These observations include the formation and evolution of a droplet-type morphology. In addition, the time evolution of the maximum value of the structure factor $S(k_m,t)$ exhibits an exponential growth during the early stage but saturates during the intermediate stage of SD. Moreover, the dominant dimensionless wavenumber k_m* decreases during the intermediate stage. The numerical results, however, also indicate that k_m* increases during the early stage, which has not yet been observed experimentally. Furthermore, the morphological analysis is also consistent with experimental observations. The droplet size and shape distributions indicate that the average droplet size and shape prevail during the PIPS phenomena, and statistical analysis of the Voronoi polygons indicates that the droplets are randomly positioned within the matrix. Lastly, the characteristic time τ, average dimensionless equivalent droplet diameter $\langle d^*\rangle$, and droplet number density N_d depend on the magnitudes of a scaled diffusion coefficient D for phase separation and a scaled rate constant K_1 for polymerization. Consistent with experimental observations, τ and $\langle d^*\rangle$ decrease while N_d increases as K_1 increases. Similarly, as D increases, τ and $\langle d^*\rangle$ decrease while N_d increases. The parameters K_1 and D have no effect on the average shape factor.

1. Introduction

The polymerization-induced phase separation (PIPS) method[1] is a novel and practical way of forming binary composite materials. This method is more complex than the more common thermal-induced phase separation (TIPS) method, where there is only phase separation occurring after a quench into the unstable region. In the PIPS method, on the other hand, phase separation and polymerization occur simultaneously. This method is best described as follows. Initially, a binary homogeneous solution consisting of monomers and a low molecular weight solvent is formed; i.e., the binary solution is in the one-phase region of its phase diagram. Typically, the binary solution exhibits an upper critical solution temperature (UCST)-type phase diagram. The monomers polymerize upon photoinitiation[2−5] or thermal initiation.[4,6−10] At some point during polymerization, phase separation occurs through spinodal decomposition (SD)[11] in the unstable region, since the solvent becomes increasing immiscible with increasing polymer chain length. While the solution undergoes phase separation, polymerization continues to produce branching. This leads to cross-linking and, eventually, gelation and the formation of a three-dimensional network that pins the phase-separated structure. At this point, the viscosity is infinite which prohibits molecular movement.

The dynamics of SD in binary polymer solutions[12−18] and blends[19−22] due to thermal quenching has been studied numerically[12−14,19,20] and experimentally.[15−18,21,22] After a thermal quench into the unstable region, two significantly different phase-separated structures can form and evolve. If the initial concentration is the critical one, an interconnected structure forms. It consists of a phase, which is rich in one of the two components, interwoven in a matrix that is rich in the other component. On the other hand, if the concentration is not the critical one but is still within the unstable region, a droplet-type morphology forms. It consists of nearly spherical droplets rich in one of the components distributed in a matrix that is rich in the other component. The droplets are fairly uniform in size and shape, and randomly distributed within the matrix.

One typical application of the PIPS method is in the formation of polymer dispersed liquid crystals (PDLCs).[1−10,23] By fabricating these composite materials as thin films on the order of 50 μm, they can be used as light shutters because of their excellent electrooptical properties. These properties include, to just name a few of them, a low switching voltage, short turn on and turn off times, and high off-state scattering efficiency.[24] They are dependent on the droplet size, shape, and/or positional order in the polymer matrix. The switching voltage is the voltage required to switch the film from the opaque state to the transparent state. The time it takes for this to happen is the turn on time, and it is proportional to the switching voltage.[25] The switching voltage increases in value as the droplet is distorted (i.e., elongated) from a perfect sphere[26] but decreases as the droplet size increases.[3] The turn off time is the time required for the transparent film in the on-state to return to being opaque after the applied voltage is removed. It increases with droplet size[3] but decreases as the droplet distorts from sphericity.[26] The scattering efficiency depends on the droplet size and positional order. Small droplets have higher contrast, which is the ratio of on-state to off-state light transmission, than large droplets. This is due to the fact that the higher droplet number density possible for small droplet sizes permits multiple light scattering in the off-state.[3] Moreover, for multiple light scattering, the droplets must not be ordered; i.e., they must be dispersed randomly in the polymer matrix. The film is opaque in its natural state but becomes transparent by applying a small voltage of 10−100 V across it. Some commercial devices making use of this new technology are switch-

---

⊗ Abstract published in *Advance ACS Abstracts,* March 1, 1997.

able windows, billboards, and color projectors. The phase-separated structure consists of liquid crystalline droplets dispersed randomly in a solid polymer matrix. In addition, the droplets are nearly spherical[24,25] with dimensions on the order of 0.1−10 μm. The actual mean dimension depends on parameters that affect phase separation and polymerization. It is noted that this description of the phase-separated structure fits the droplet-type morphology described above. Although the interconnected structure, or variations of it such as the polymer ball morphology,[4] is also a possible candidate for the phase-separated structure in PDLCs, it is generally not useful for electrooptical applications and will not be considered in this paper. Phase separation studies of both the PIPS[5,7−9] and TIPS[5,7] methods indicate that PDLCs are formed by SD.

The industrial importance of PDLC films[27] provided us with the initiative to investigate further the PIPS method of fabricating these thin films, despite the fact that others have already provided some insights into the PIPS method of fabricating PDLCs[5,7−9,28−30] and polymer blends.[31−34] In our previous paper,[35] we presented results from a numerical study of PDLC film formation using the PIPS method. An emphasis was placed on the intimate coupling between phase separation and polymerization processes on the droplet size selection mechanism during film fabrication. The numerical results replicate frequently reported experimental observations. For instance, the time evolution of the maximum value of the structure factor, which is a complex function of the amount and length scale of phase separation, is in accordance with experimental observations on the formation of PDLCs by the PIPS method. It grows exponentially during the early stage but eventually saturates as the phase separation enters the intermediate stage of SD. Furthermore, a transient periodic phase-separated structure develops and evolves. The existence of a maximum value of the structure factor at any time during phase separation is consistent with the formation of a transient periodic phase-separated structure. We also showed in the computational analysis that the selected transient wavelength must satisfy the complex competing effects of the polymerization and phase separation processes. Each process is characterized by a scaled parameter, which is a scaled rate constant K_1 for polymerization and a scaled diffusion coefficient D for phase separation. In addition to the characteristic length scale, both parameters also affect the characteristic time scale defined to be the induction time, which is the sum of the polymerization and phase separation lag times. As K_1 increases, the dominant wavenumber also increases but the polymerization lag time decreases. Similarly, as D increases, the dominant wavenumber also increases but the phase separation lag time decreases. On the basis of these two scaled parameters, the dominant wavelength selection mechanism in the PIPS process was identified. This understanding between the competitive interactions of the two processes allows the droplet size to be controlled to specifications during PDLC film fabrication.

The next step after understanding the droplet size selection mechanism is to perform a morphological analysis of the phase-separated structure. An appropriate analysis is a quantitative description of the sizes, shapes, number density, and positional correlation of the droplets.[36] This defines the scope of this paper, which is a continuation of our previous paper[35] on the droplet size selection mechanism in the PIPS method. The specific objective of this paper is to present results from a two-dimensional numerical study on the isothermal phase separation phenomena during the polymerization of a model binary trifunctional monomer−small molecule solvent solution. With increasing polymer molecular weight, it is assumed that the solute remains monodisperse and phase separation occurs in the unstable region of the binary phase diagram. The nonlinear Cahn−Hilliard (C−H) equation[11,37,38] and Flory−Huggins (F−H) free energy equation[39,40] are used to describe the phase separation phenomena. The self-condensation polymerization is assumed to follow second-order kinetics. Since this paper is an extension of our previous one, we are still interested in the effect of the competition between the phase separation and polymerization processes on the formation of droplets in PDLCs. Consequently, the numerical study is restricted to the dynamics of the phase-separated structure during the early stage and beginning of the intermediate stage of SD. An emphasis is placed, however, on a morphological analysis of the transient phase-separated structure. A description of the droplet sizes and shapes makes use of a statistical analysis of the equivalent droplet diameter and shape factor, respectively. By determining the center of gravity of each droplet, Voronoi polygons can be constructed by applying the Dirichlet tessellation method to these centers. A statistical analysis of these polygons will then determine if the droplets are randomly dispersed. The droplet number density is defined to be the number of droplets per unit area.

The rest of this paper is organized as follows. The model and method of solution are described briefly in Section 2. The numerical results are presented, discussed, and contrasted with experimental data in Section 3. Lastly, conclusions are given in Section 4.

2. Problem Formulation and Numerical Methods

Since the problem formulation and numerical methods are described in detail in our previous papers,[12,13,35] only a concise description of them is given here.

2.1. Theory. The PIPS method is a complex combination of the polymerization and phase separation processes. The essence of each process is described briefly below.

Phase separation in the unstable region of the binary phase diagram can be described using the nonlinear C−H equation.[11,37,38] It is derived from the continuity equation, where the mobility M is the ratio of the negative flux to the gradient of the functional derivative of the total free energy. The total free energy contains two terms. The first term is the volume integral of a homogeneous free energy density. An appropriate choice for both monomer and polymer systems is the F−H free energy density,[39,40] since it takes into account the degrees of polymerization N_1 and N_2 of the solvent and solute, respectively. For polymer solutions, it is usually assumed that $N_1 = 1$. Furthermore, the F−H free energy density is suitable for phase separation studies because it can have one or two local minima. The second term takes into account any increases in free energy due to concentration gradients. It is the volume integral of the product of the parameter related to the interfacial tension κ and the square magnitude of the solvent concentration gradient.

Both M and κ are dependent on the polymer molecular weight (or N_2), which is continuously increasing with time in the PIPS method. Their dependencies, however, can only be approximated since there is cross-linking and network formation. The entanglements of the polymer chains in a polymer melt resemble closely the branching and cross-linking that occur during the PIPS method. Consequently, the molecular weight dependence of M can be approximated by applying the Stokes−Einstein equation[41] to a polymer melt. Empirical equations are given in the literature relating polymer melt viscosity to the number of backbone atoms.[40,42] The relation

$M = M_o N_2^{-1}$ is then obtained for the self-condensation of a trifunctional monomer during the early and intermediate stages of SD where $N_2 < 300$. This functional dependence of M on N_2 is appropriate for the present system because cross-linking hinders molecular movement. The limiting case occurs at gelation ($N_2 \rightarrow \infty$), where the viscosity is infinite and no molecular movement is allowed. The parameter κ is comprised of an enthalpic term and an entropic term.[43] For small molecule systems and polymer solutions, only the enthalpic term is important. It is the product of Flory's interaction parameter χ and the square of the interaction length l_i between the molecules. For polymer solutions, this length is the radius of gyration R_g.[44] Even though the solution in the present study consists of branched polymer molecules, it is assumed that $l_i = R_g$. Since the radius of gyration of a nonlinear polymer is a fraction of that for a linear polymer of the same molecular weight,[39] $\kappa = \kappa_o N_2$. Consequently, as the polymer chain grows, so does its interaction with the solvent.

The phase separation phenomenon is usually followed experimentally by light, X-ray, or neutron scattering. The scattering pattern consists of a bright ring in a dark background. During phase separation, the brightness intensifies but the ring radius decreases. Numerical results, however, are usually compared to time-resolved scattering intensity profiles $I(\mathbf{s},t)$, where $\mathbf{s}$ is the scattering wavevector. The comparison is made between $I(\mathbf{s},t)$ and the structure factor $S(\mathbf{k},t)$, which is defined to be the square magnitude of the Fourier transform of the concentration fluctuations, for $\mathbf{s} = \mathbf{k}$.[45]

The polymerization kinetics for the self-condensation of a trifunctional monomer A_3 is described by the conventional rate equation.[46] Since the condensation reaction is bimolecular, the rate equation is second order. The weight-average $\langle X_w \rangle$ and number-average $\langle X_n \rangle$ degrees of polymerization are obtained from the molecular size distribution functions.[39,47] The degrees of polymerization are expressed in terms of the branching coefficient α, which is defined as the probability that a randomly chosen functional group of a branch unit is connected to another branch unit. For the single-reactant system A_3, $\alpha = p$, where p is the extent of reaction and is obtained from the analytical solution of the rate equation. In addition, at the gel point, where $\alpha = 0.5$, $\langle X_w \rangle \rightarrow \infty$ while $\langle X_n \rangle = 4$. Since $\langle X_w \rangle$ better reflects the molecular weight growth leading to the formation of an infinite network, it is used in this study to represent the solute degree of polymerization; i.e., $N_2 = \langle X_w \rangle$.

2.2. Governing Equations and Auxiliary Conditions. This paper is restricted to a two-dimensional numerical study of the PIPS of a monomer–solvent solution confined to a square with dimensions L. It is assumed, that as the phase diagram shifts upward in the temperature T–solvent concentration c plane during polymerization, the metastable region crosses the initial (c,T) conditions at a sufficiently high speed such that nucleation is not possible. Consequently, the phase separation is solely SD and is governed by the nonlinear C–H and F–H equations. It is assumed that the mobility M and interfacial parameter κ in the C–H equation are functions of the solute degree of polymerization N_2, while the interaction parameter χ in the F–H equation is a function of T only. The interaction parameter is related to T through an expression containing the theta temperature θ and dimensionless entropy of dilution parameter ψ.[39,40] Furthermore, it is assumed that the solute is always monodisperse at any degree of polymerization N_2, while the solvent degree of polymerization N_1 remains unity at all times. Hydrodynamic effects are not considered because they are only important during the late stage of SD in concentrated polymer solutions,[15] which is beyond the time range of interest in this paper. It is also assumed that the glass transition temperature T_g versus concentration curve remains above the binodal line throughout the polymerization process. This is plausible since T_g increases with cross-linking. The self-condensation of A_f, with functionality $f = 3$, follows second-order kinetics with rate constant k_1. Although polymerization occurs independently of phase separation in this study, phase separation depends on polymerization by the presence of N_2 in the F–H equation.

The derivation of the governing equations and auxiliary conditions is in our previous paper.[35] The derivation of the phase separation governing equation in two dimensions is similar to that in one dimension, since the only differences occur in additional spatial derivatives. Consequently, the dimensionless fourth-order nonlinear partial differential equation governing the phase separation process and the dimensionless algebraic equation governing the polymerization process are, respectively, as follows:

$$\frac{\partial c^*}{\partial t^*} = \frac{DT^*}{N_2}\left[-\frac{1}{c^{*2}} + \frac{1}{N^2}\frac{1}{(1 - c^*)^2}\right]\left[\frac{\partial c^*}{\partial x^*}\frac{\partial c^*}{\partial x^*} + \frac{\partial c^*}{\partial y^*}\frac{\partial c^*}{\partial y^*}\right] + \frac{DT^*}{N_2}\left[\frac{1}{c^*} + \frac{1}{N_2}\frac{1}{(1 - c^*)} - 2\chi\right]\left[\frac{\partial^2 c^*}{\partial x^{*2}} + \frac{\partial^2 c^*}{\partial y^{*2}}\right] - \left[\frac{\partial^4 c^*}{\partial x^{*4}} + 2\frac{\partial^4 c^*}{\partial x^{*2}\partial y^{*2}} + \frac{\partial^4 c^*}{\partial y^{*4}}\right] \quad (1a)$$

$$N_2 = \frac{1 + 2K_1 t^*}{1 + 2K_1 t^* - fK_1 t^*} \quad (1b)$$

which are defined for $t^* > 0$ and for the unit square $0 \leq x^* \leq 1$, $0 \leq y^* \leq 1$. The superscripted asterisks denote dimensionless variables. In eq 1, $x^* = x/L$, $y^* = y/L$, $T^* = T/\theta$, $c^* = c$, $t^* = 2M_o\kappa_o t/L^4$, $D = (k_B\theta L^2/2\nu\kappa_o)\cdot(\text{molecule/segments})^2$, and $K_1 = k_1 L^4/2M_o\kappa_o$. According to the F–H theory, k_B is Boltzmann's constant and v is the volume of a cell or segment. Two parameters are obtained in the nondimensionalization process. The dimensionless diffusion coefficient D controls the rate of phase separation, while the dimensionless rate constant K_1 controls the rate of polymerization.

An appropriate initial condition for eq 1a is one that captures the infinitesimal concentration fluctuations that are present in a homogeneous binary solution at thermal equilibrium. These are the fluctuations that are needed for SD and are assumed to be present immediately after the binary solution is thrust into the unstable region during polymerization. The initial value of c^* is given by the following dimensionless expression:

$$c^*(x^*,y^*,t^* = 0) = c_o^* + \sum_{m=1}^{64}\sum_{n=1}^{64} c_{mn}^* \sin(m\pi x^* + \varphi x)\sin(n\pi y^* + \varphi_y) \quad (2)$$

where c_o^* is the average dimensionless concentration. Furthermore, c_{mn}^* is the square root of the thermally averaged square of the dimensionless concentration fluctuation amplitude of Fourier modes m and n, and φ_x and φ_y are random phases. The range of m and n in this study is restricted to m, $n = 1, 2, ..., 64$, which provides sufficient Fourier modes. For each value of m and n, a Monte Carlo scheme[48] is used to determine an amplitude c_{mn}^* and two random phases.

Two sets of boundary conditions are required in this study. The first set is obtained by noting that there is no mass exchange with the surroundings,[49] and it is expressed as follows in dimensionless form:

$$\frac{\partial^3 c^*}{\partial x^{*3}} + \frac{\partial^3 c^*}{\partial x^* \partial y^{*2}} = 0 \text{ at } t^* > 0 \text{ and } x^* = 0 \text{ and } 1 \quad (3a)$$

$$\frac{\partial^3 c^*}{\partial y^{*3}} + \frac{\partial^3 c^*}{\partial y^* \partial x^{*2}} = 0 \text{ at } t^* > 0 \text{ and } y^* = 0 \text{ and } 1 \quad (3b)$$

The second set of boundary conditions is obtained by evaluating the functional derivative of the total free energy[38] and is expressed as follows in dimensionless form:

$$\frac{\partial c^*}{\partial x^*} = 0 \text{ at } t^* > 0 \text{ and } x^* = 0 \text{ and } 1 \quad (4a)$$

$$\frac{\partial c^*}{\partial y^*} = 0 \text{ at } t^* > 0 \text{ and } y^* = 0 \text{ and } 1 \quad (4b)$$

In summary, the dependent variables are c^* and N_2, and the independent variables are x^*, y^*, and t^*. While eq 1b is an analytical solution to the ordinary differential equation

Table 1. Dimensionless Material Parameter Values and Results for Simulation of Polymerization-induced Spinodal Decomposition[a]

case[b]	K_1	D (10^5)	τ	$N_2(\tau)$	$\langle d^*(\tau)\rangle$	$\langle S_f(\tau)\rangle$	$N_d(\tau)$
A	10	1	4930.71	3.92	0.45	0.87	2.25
B	100	1	509.25	4.11	0.28	0.90	6.25
C	1000	1	54.58	4.61	0.22	0.83	10.25
D	10	2	4881.49	3.86	0.40	0.90	2.75
E	100	2	497.82	3.97	0.25	0.89	7.50
F	1000	2	51.96	4.25	0.20	0.85	13.75
G	10	4	4852.64	3.83	0.35	0.89	3.00
H	100	4	491.10	3.90	0.22	0.88	9.00
I	1000	4	50.40	4.05	0.17	0.85	17.25

[a] The material parameters are the dimensionless rate constant K_1 and dimensionless diffusion coefficient D. The results are the solute degree of polymerization $N_2(\tau)$, the average dimensionless equivalent diameter of the solvent-rich nearly circular regions $\langle d^*(\tau)\rangle$, the average shape factor $\langle S_f(\tau)\rangle$, and the droplet number density $N_d(\tau)$ at the characteristic time τ. [b] For all cases, $c_o^* = 0.6$, $T^* = 0.6$, $\chi = 1.1667$, and $\psi = 1$.

describing the polymerization process, there is none for the phase separation process. Therefore, eqs 1a and 2–4 must be solved numerically for $c^*(x^*,y^*,t^*)$. The parameters are the dimensionless rate constant K_1, the dimensionless diffusion coefficient D, the average dimensionless concentration c_o^*, the dimensionless temperature T^*, and the interaction parameter χ. Recall that χ is related to T^* through an expression containing θ and ψ, where in this study $\psi = 1$. Although a comprehensive parametric study was performed on D, c_o^*, T^*, and K_1, the limited number of simulation results presented here best reflect the objectives of this paper. Table 1 lists the parameter values used in the nine simulations presented in this paper. The coordinates (0.6,0.6) represent a typical experimental curing point on a binary phase diagram and in particular for PDLCs formed by the PIPS method.[1,6–9] In other words, the curing point is in the one-phase homogeneous region initially, but then it enters and remains in the unstable region at some point during polymerization. Moreover, the values for D and K_1 listed in Table 1 are appropriate for a parametric study. At one extreme (low D and K_1) little phase separation occurs, but at the other extreme (high D and K_1) significant phase separation is present.

2.3 Integration Method. Eqs 1a and 2–4 are solved numerically by using the finite element method for spatial discretization.[50] Hermitian bicubic interpolants are used here as basis functions since they are appropriate for the numerical solution of fourth-order partial differential equations.[51,52] In addition, Hermitian bicubic interpolants incorporate easily the zero mass flux and natural boundary conditions used in this study.[12] After spatial discretization, a set of nonlinear time-dependent ordinary differential equations are obtained,[12] which must be solved simultaneously. The Newton–Raphson iteration method is used for this purpose, and convergence is assumed to occur when the length of the vector of the difference of two successive computed solution vectors is less than 10^{-6}.

A finite difference method is used to discretize time, and a first-order implicit Euler predictor–corrector method is used to integrate time. An adaptive time controller scheme is incorporated into the computations so that the computing time is minimized.[53] The essence behind this scheme is that large (small) time steps are used when little (significant) changes occur in the transient solution. To accomplish this task, it takes into account the local truncation error and a user-specified tolerance.

The numerical results presented in this paper were obtained from simulations performed on a CRAY C98/8256 supercomputer using a mesh consisting of 32 × 32 nodes.

3. Results and Discussion

The results and discussion presented below in Sections 3.1, 3.2, and 3.4 are for case I in Table 1. It must be noted, however, that the results for case I are typical of all cases in Table 1. Therefore, the discussion is applicable to all cases in Table 1.

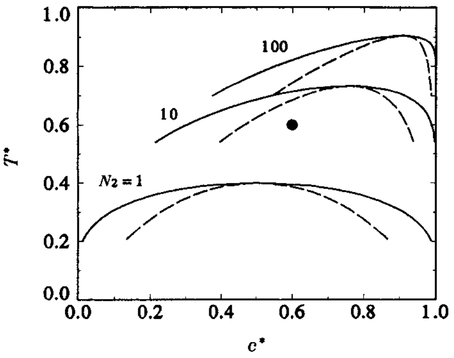

Figure 1. Binary phase diagrams for $N_1 = 1$ and, from bottom to top, $N_2 = 1$, 10, and 100. They are calculated using Flory–Huggins free energy density with $\psi = 1$. The solid curves are the binodal lines, while the dashed curves are the spinodal lines. The dot at coordinates (0.6, 0.6) represents the curing point. These three degrees of polymerization are chosen solely to illustrate the continuous effect that polymerization has on the phase diagram. Initially, the system is a monomer solution with a symmetric phase diagram; i.e., $N_1 = N_2 = 1$. During polymerization, N_2 continuously increases with time, the phase diagram becomes asymmetric, and the curing point is thrust into the unstable region where phase separation occurs by spinodal decomposition. Once the curing point enters the unstable region, it remains there throughout the polymerization.

3.1. Representative Phase-separated Structures and Patterns. Figure 1 is a plot of dimensionless temperature T^* versus dimensionless solvent concentration c^* calculated using the Flory–Huggins theory.[12] For illustrative purposes on the effect polymerization has on the binary phase diagram, only phase diagrams at degrees of polymerization $N_2 = 1$, 10, and 100 are shown. For each N_2 value, the solvent degree of polymerization is unity; i.e., $N_1 = 1$. The solid curves represent the binodal lines, while the dashed curves are the spinodal lines. The dot at coordinates (0.6,0.6) represents the curing point for which results will be presented and discussed in this paper. Initially, $N_2 = 1$ and the monomer–solvent solution is in the one-phase homogeneous region. During polymerization, the phase diagram shifts continuously toward higher coordinates. After some time, the spinodal line crosses the curing point. The time that it takes for this to happen is called the dimensionless polymerization lag time t_o^*. For $t^* > t_o^*$, the curing point remains in the unstable region and the solution undergoes phase separation through SD.

Shown in Figure 2 is a plot of the initial dimensionless solvent concentration spatial profile $c^*(x^*,y^*,t^* = 0)$ for case I in Table 1. It was calculated from Monte Carlo simulations using eq 2. This profile represents the infinitesimal thermal concentration fluctuations that are present in a binary homogeneous solution at thermal equilibrium and are required for SD to take place. As shown in this figure, these fluctuations are extremely random and have a maximum amplitude of only 10^{-6}. Similar random initial conditions are used for the other simulations listed in Table 1.

Figure 3 shows the dimensionless concentration spatial profiles $c^*(x^*,y^*)$ (first column) and patterns (second column) formed during the phase separation phenomena for case I at the following dimensionless times: $t^* = 50.08 \times 10^{-5}$ (first row), $t^* = 50.19 \times 10^{-5}$ (second row), $t^* = 50.43 \times 10^{-5}$ (third row), and $t^* = 51.27 \times 10^{-5}$ (fourth row). The black regions (white regions) are solvent-rich regions (solute-rich regions), where $c^* > c_o^*$ ($c^* < c_o^*$). The time evolution of the patterns indicates that a droplet-type morphology forms and evolves during the phase separation phenomena from the random

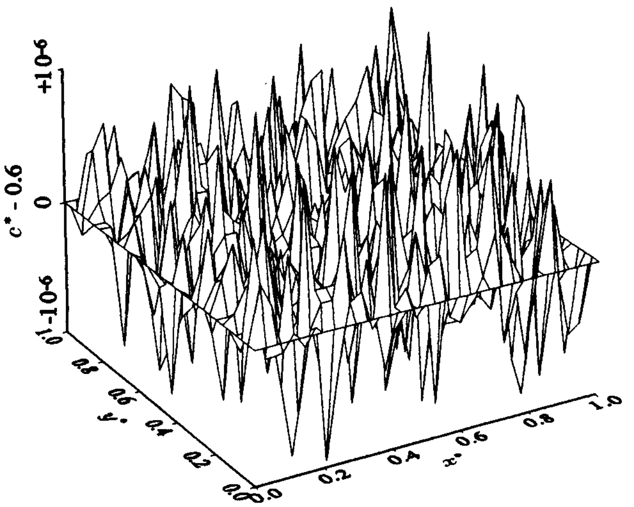

Figure 2. Initial dimensionless concentration spatial profile $c^*(x^*,y^*)$ corresponding to case I in Table 1. It represents the infinitesimal concentration fluctuations that are present in a binary solution at thermal equilibrium. The surface was computed using a Monte Carlo technique. The dimensionless average concentration is $c_0^* = 0.6$, and the maximum amplitude is 10^{-6}. Notice that $c^*(x^*,y^*)$ is very random initially.

initial condition shown in Figure 2. This is expected for two reasons. Firstly, the dimensionless average solvent concentration c_0^* remains an off-critical one at all times during the phase separation phenomena. Recall that a droplet-type morphology (interconnected structure) forms at off-critical (critical) concentrations after a thermal quench into the unstable region of the binary phase diagram. Secondly, the value of c_0^* used in this paper is close to the one used in fabricating PDLCs,[1,6-9] which consist of liquid crystalline droplets dispersed uniformly in a polymer matrix. In addition, the time evolution of the patterns indicates that the random initial condition shown in Figure 2 develops initially into a phase-separated structure resembling to some extent the droplet-type morphology with a low droplet number density N_d (see pattern at $t^* = 50.08 \times 10^{-5}$). The number density increases during the PIPS phenomena (see pattern at $t^* = 50.19 \times 10^{-5}$), but at some point N_d decreases (see patterns at $t^* = 50.43 \times 10^{-5}$ and 51.27×10^{-5}). This can be explained as follows. After the dimensionless induction time t_i^*, phase separation begins. At this time the quench depth, defined as the absolute difference between the critical and curing temperatures $|T_c - T|$, is shallow. Accordingly, the average equivalent droplet diameter $\langle d \rangle$ is large and N_d is low (see pattern at $t^* = 50.08 \times 10^{-5}$). Note that this result illustrates the inverse relationship between d and N_d. During polymerization, the phase diagram shifts toward higher temperatures and concentrations. This effectively increases the quench depth, thereby resulting in smaller d and higher N_d values (see pattern at $t^* = 50.19 \times 10^{-5}$). The spatial profile at $t^* = 50.19 \times 10^{-5}$ shows that the concentration gradient at the interfaces is large. This increases the total free energy of the system through the κ term of the total free energy expression used to derive the C–H equation. Consequently, this term represents the resisting force against phase separation. To reduce this energy increase, the droplet-type morphology coarsens to minimize the interfacial area. This is seen in the patterns at $t^* = 50.43 \times 10^{-5}$ and 51.27×10^{-5}, where N_d is decreasing while the remaining droplets are increasing slightly in size. This type of coarsening process is in accordance with evaporation–condensation theory.[54]

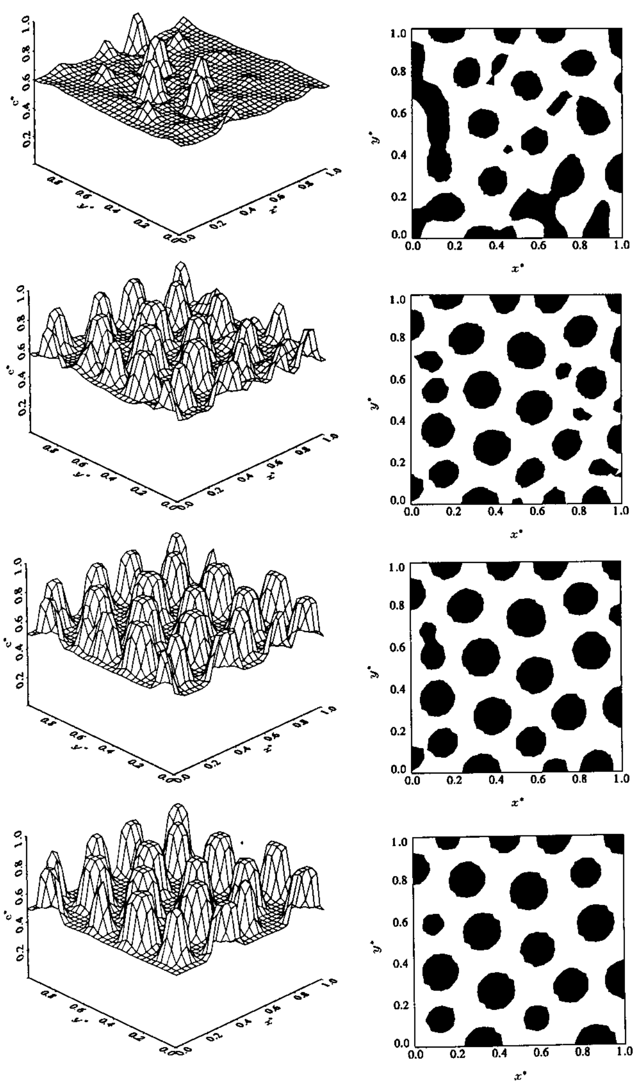

Figure 3. Dimensionless concentration spatial profiles $c^*(x^*,y^*)$ (first column) and patterns (second column) formed during the phase separation phenomena for the simulation corresponding to case I at the following dimensionless times: $t^* = 50.08 \times 10^{-5}$ (first row), $t^* = 50.19 \times 10^{-5}$ (second row), $t^* = 50.43 \times 10^{-5}$ (third row), and $t^* = 51.27 \times 10^{-5}$ (fourth row). The black regions (white regions) in the patterns represent solvent-rich regions (solute-rich regions) with $c^* > c_0^*$ ($c^* < c_0^*$), where $c_0^* = 0.6$ is the dimensionless average concentration. Notice that the phase-separated structure develops into a droplet-type morphology, which is typically observed in polymerization-induce spinodal decomposition.

Results can not be presented for $t^* > 51.27 \times 10^{-5}$ because the computations fail to converge at $t^* \cong 52.00 \times 10^{-5}$. This problem is typical of phase separation in binary polymer solutions with highly asymmetric phase diagrams and occurs when c^* at any mesh point approaches unity. We have already addressed this problem in a previous paper.[13] In addition, this problem does not preclude us from achieving our objective, since it occurs beyond the time range of interest in this paper, which corresponds to the early and intermediate stages of SD.

Figure 4 is a plot of the circularly averaged structure factor $S(k^*,t^*)$ versus dimensionless wavenumber k^* at the following dimensionless times: $t^* = 50.08 \times 10^{-5}$ (dotted line), $t^* = 50.19 \times 10^{-5}$ (solid line), $t^* = 50.43 \times 10^{-5}$ (short dashed line), and $t^* = 51.27 \times 10^{-5}$ (long dashed line). Note that these are the same four t^*'s as in Figure 3. The method of determining the structure factor and its circular average is described in one of our previous papers.[13] Moreover, the time evolution of

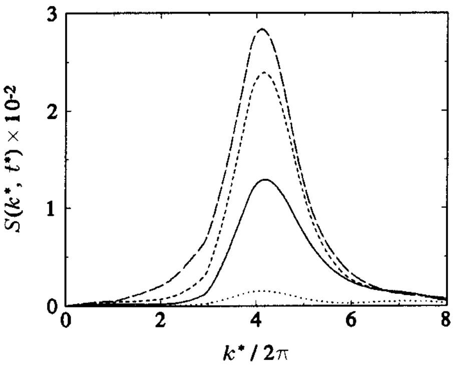

Figure 4. Circularly averaged structure factor $S(k^*,t^*)$ versus the dimensionless wavenumber k^* for the simulation corresponding to case I. The dimensionless times are: $t^* = 50.08 \times 10^{-5}$ (dotted line), $t^* = 50.19 \times 10^{-5}$ (solid line), $t^* = 50.43 \times 10^{-5}$ (short dashed line), and $t^* = 51.27 \times 10^{-5}$ (long dashed line). These results correspond to those shown in Figure 3. The location of $S(k_m^*,t^*)$ is fairly constant during the time range of interest in this study, indicating that the phase separation phenomena results are in the early stage and beginning of the intermediate stage of spinodal decomposition.

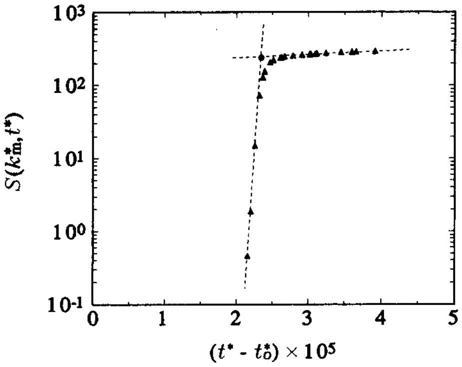

Figure 5. Maximum structure factor $S(k_m^*,t^*)$ as a function of dimensionless time $(t^* - t_o^*)$ for the simulation corresponding to case I. This curve is typical of spinodal decomposition, since the initial exponential growth eventually slows down and saturates. The dashed lines are tangents along each part of the curve, and their intersection, located by the dot, indicates the transition point between the early and intermediate stages of spinodal decomposition.

$S(k^*,t^*)$ is consistent with the time evolution of the spatial profiles and patterns shown in Figure 3 and described above. One such consistency is in the length scale. The value of k_m^*, which is the dimensionless wavenumber where the maximum of $S(k^*,t^*)$ is located, increases at first but eventually decreases. Note that $k_m^* = 2\pi/\lambda_m^*$, where λ_m^* is the dimensionless dominant wavelength of the periodic phase-separated structure. It can be assumed that $\lambda_m^* \propto \langle d^* \rangle$. Consequently, $\langle d^* \rangle$ decreases while N_d increases as k_m^* increases. The other consistency is in the amount of phase separation, which is indicated by $|c^* - c_o^*|$. The spatial profiles in Figure 3 show that $|c^* - c_o^*|$ is increasing with time, and this is captured in Figure 4 with $S(k_m^*,t^*)$, which is the structure factor $S(k^*,t^*)$ evaluated at k_m^*, increasing with time. Therefore, the circularly averaged structure factor is a complex function of k_m^* and $|c^* - c_o^*|$, and this is the reason why light, X-ray, or neutron scattering is used to follow SD.

Figure 5 shows a semilogarithm plot of the maximum structure factor $S(k_m^*,t^*)$ versus $(t^* - t_o^*)$ corresponding to case I. In this figure, the dashed lines are tangents to each part of the curve, and their intersection, located by the dot at $(t^* - t_o^*) = 2.33 \times 10^{-5}$, gives the transition point between the early and intermediate stages of SD. The dimensionless polymerization lag time is calculated from the following expression:[35]

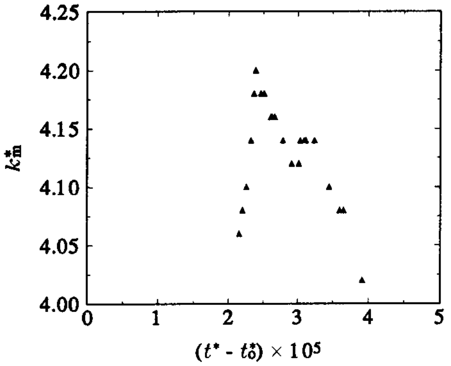

Figure 6. Dimensionless wavenumber where the circularly averaged maximum structure factor is located versus dimensionless time $(t^* - t_o^*)$ for the simulation corresponding to case I. The transition between the early and intermediate stages of spinodal decomposition is at the apex. In the early stage k_m^* increases, but in the intermediate stage it generally decreases.

$$t_o^* = \frac{\alpha}{K_1(1 - \alpha)} \tag{5}$$

where $\alpha \cong 0.3235$ when the unstable region crosses the curing point on the binary phase diagram. The transition point is then the dimensionless transition time t_t^* and $S(k_m^*,t_t^*)$, which is the value of $S(k_m^*,t^*)$ at t_t^*. An additional feature of this plot is that $S(k_m^*,t^*)$ grows exponentially during the early stage, but then slows down as the phase separation enters the intermediate stage. This feature has been observed experimentally in PDLCs[8,9] and other polymer systems[31-33] formed by the PIPS method. Consequently, the time range of interest in this paper is the early stage and beginning of the intermediate stage of SD. Furthermore, the time evolution of $S(k_m^*,t^*)$ during the PIPS process is then similar to that observed in the TIPS process in the time range explored in this study.[13] Lastly, Figure 5 shows that there is a dimensionless induction time $t_i^* = t_o^* + t_c^*$, where t_o^* and t_c^* are, respectively, the dimensionless polymerization and phase separation lag times. This is observed in Figure 5 since significant phase separation, which is measured by the magnitude of $S(k_m^*,t^*)$, only occurs at $(t^* - t_o^*) > 0$. There is a phase separation lag time, which is similar to the one identified in the TIPS process,[12] because $(t^* - t_o^*) > 0$.

Figure 6 is a plot of k_m^* versus $(t^* - t_o^*)$ corresponding to case I. The transition point obtained in Figure 5 coincides with the apex in Figure 6. Consequently, the trend in Figure 6 shows that k_m^* increases with time during the early stage but then generally decreases with time during the early part of the intermediate stage. The decrease during the intermediate stage is consistent with experimental observations in the formation of PDLCs by the PIPS method.[8,9] On the other hand, the increase during the early stage has apparently not been observed experimentally in the formation of PDLCs by the PIPS method. A plausible reason for this is that the phase separation dynamics is too fast to be captured experimentally at early times. As shown in Figure 6, the increase in k_m^* in the early stage is due to the large irregular shape regions forming the interconnected structure pinching to form droplets. A comment must be made about the numerical values of k_m^*. They are obtained from the calculations of the circularly averaged structure factor, where only a fixed finite number of wavenumbers is used. Therefore, the location of the

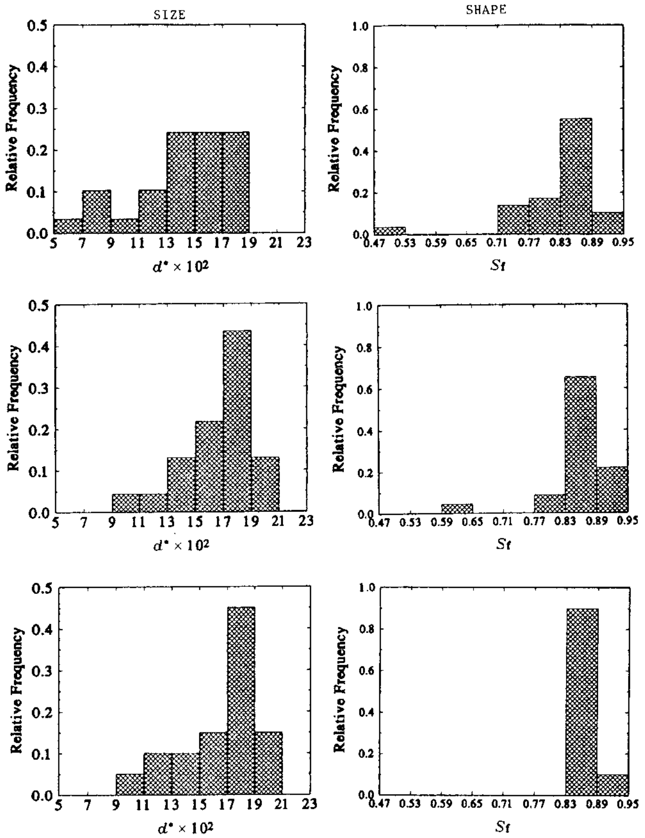

Figure 7. Frequency histograms of the dimensionless equivalent diameter of the solvent-rich nearly circular regions d^* (first column) and the shape factor S_f (second column) for the simulation corresponding to case I. The dimensionless times are as follows: $t^* = 50.19 \times 10^{-5}$ (first row), $t^* = 50.43 \times 10^{-5}$ (second row), and $t^* = 51.27 \times 10^{-5}$ (third row). These results correspond to those shown in Figure 3. With time, the droplets become almost uniform in size and shape.

maximum of $S(k^*,t^*)$, which is k_m^*, is only approximate. This explains why k_m^* is constant for some time ranges and increases slightly at $(t^* - t_o^*) \cong 3.0 \times 10^{-5}$ to 3.5×10^{-5} in Figure 6. Nevertheless, the overall trend is apparent and consistent with the aforementioned discussion about Figure 3.

3.2. Representative Droplet Size and Shape Distributions. Information about the droplet size and shape distributions can be obtained by drawing frequency histograms of the parameters describing these two droplet features. Figure 7 shows frequency histograms for the dimensionless equivalent diameter of the solvent-rich nearly circular regions d^* (first column) and the shape factor S_f (second column) at the following dimensionless times: $t^* = 50.19 \times 10^{-5}$ (first row), $t^* = 50.43 \times 10^{-5}$ (second row), and $t^* = 51.27 \times 10^{-5}$ (third row). Once more, these results correspond to case I. The shape factor is defined as $S_f = 4\pi A/P^2$, where A and P are, respectively, the area and perimeter of the nearly circular droplets, and is a measure of how circular a droplet is. The two extreme values belong to a perfect circle where $S_f = 1$ and to a line where $S_f \rightarrow 0$. Moreover, the dimensionless equivalent diameter is defined as $d^* = (4A/\pi)^{1/2}$. The time evolution of the histograms for d^* and S_f indicates that the phase-separated structure evolves gradually from one containing a wide distribution of droplet sizes and shapes (first row) to one containing predominately one droplet size and shape range (third row). This is supported by a visual inspection of the patterns shown in Figure 3. The histograms for d^* are skewed to the left. There is, however, no consensus in the literature as to the type of histograms appropriate for the d^* distribution formed from the PIPS and TIPS methods.[4] The histograms for S_f indicate that no droplets are perfectly circular, where $S_f = 1$. The droplets in PDLCs are noncircular.[24] The distributions at $t^* = 51.27 \times 10^{-5}$ (third row) indicate that the droplet size and shape have almost no variations, since most of the droplets fall within the range of $0.17 < d^* < 0.19$ and $0.83 < S_f < 0.89$. Therefore, for all practical purposes, it can be assumed that d^* and S_f are each equal to a single unique value denoted, respectively, by the average dimensionless equivalent diameter $\langle d^* \rangle$ and average shape factor $\langle S_f \rangle$, as required in PDLCs.

3.3. Effect of Dimensionless Diffusion Coefficient and Rate Constant. Table 1 also summarizes the effects of the dimensionless rate constant K_1 and dimensionless diffusion coefficient D on the dimensionless characteristic time $\tau = 1.005 \times t_t^*$, the average dimensionless equivalent diameter $\langle d^* \rangle$, the average shape factor $\langle S_f \rangle$, and the droplet number density N_d for each of the nine cases. For each case, the parameters $\langle d^* \rangle$, $\langle S_f \rangle$, and N_d are evaluated at τ. The definition of τ given above is different from that defined in our previous paper.[35] It is redefined in this paper because the dimensionless time $1.25 \times t_t^*$, which is the definition of τ in our previous paper,[35] is greater than the dimensionless time when the convergence problem occurs. This redefinition does not cause any problems or inconsistencies because its purpose is simply to define a standard time when the droplets are to be characterized.

From Table 1, it is noticed that both τ and $\langle d^*(\tau) \rangle$ decrease as K_1 increases at constant D. The relationship between τ and K_1 can be explained using t_i^*. The dimensionless induction time is a good indicator of the magnitude of τ. It is known that t_c^* is inversely proportional to D.[12] Consequently, any variations in t_c^* between the different cases with the same D in Table 1 should be negligible. It can then be concluded that the source for any variations in t_i^* between cases with the same D in Table 1 is due to t_o^*. This explains the relationship between τ and K_1, since according to eq 5 $t_o^* \propto K_1^{-1}$. The variation of τ is also reflected in the dependence of $N_2(\tau)$ on K_1 through eq 1b and is listed in Table 1. This fact is then used to explain the relationship between $\langle d^*(\tau) \rangle$ and K_1, which has been observed experimentally.[3,6,10] According to the TIPS process, the dominant wavenumber (droplet size) increases (decreases) as N_2 increases.[35] In other words, $\langle d^* \rangle$ is inversely proportional to N_2. Even though this fact applies to the TIPS process, it can be used as an approximation for the PIPS process since the phase diagram is fixed at any given time. This approximation has already been used successfully by others[34] in the numerical study of the PIPS process. The number density increases with K_1 because, as mentioned earlier, N_d is inversely proportional to $\langle d^* \rangle$. Lastly, there does not seem to be any correlation between $\langle S_f \rangle$ and K_1, since the formation of almost spherical droplets is intrinsic to the formation of PDLCs by the PIPS method.

From Table 1, it is also noticed that both τ and $\langle d^*(\tau) \rangle$ decrease as D increases at constant K_1. As mentioned above, t_i^* is a good indicator of the magnitude of τ. When K_1 is constant, any variations in t_i^* are due to the phase separation process. It is known that t_c^* is inversely proportional to D.[12] Therefore, the relationship between τ and D shown in Table 1 reflects the effect that the magnitude of D has in the governing equation. According to eq 1a, as D increases the rate of change of c^* also increases, which means that t_c^* will decrease. This effect has already been seen in the TIPS pro-

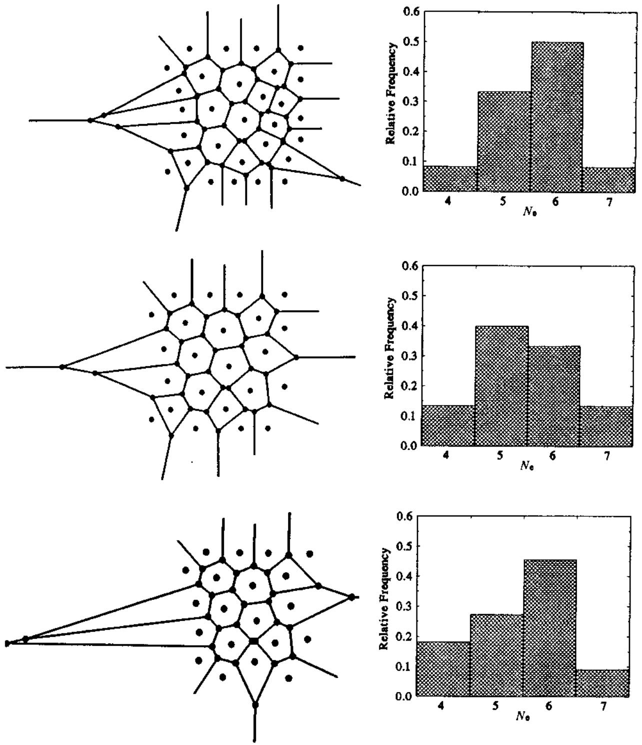

Figure 8. Dirichlet tessellations (first column) and frequency histograms of the number of edges N_e in the Voronoi polygons (second column) for the simulation corresponding to case I. The dimensionless times are as follows: $t^* = 50.19 \times 10^{-5}$ (first row), $t^* = 50.43 \times 10^{-5}$ (second row), and $t^* = 51.27 \times 10^{-5}$ (third row). These results correspond to those shown in Figure 3. Two sets of dots must be differentiated in this figure. One set of dots indicates the intersection of two edges obtained from the application of the Dirichlet tessellation method. The remaining set of dots denotes the centers of gravity of the droplets shown in Figure 3. The variation in the number of edges indicates that the droplets are randomly positioned.

cess.[12,13] The relationship between $\langle d^*(\tau)\rangle$ and D can be explained as follows. The parameter D (defined in Section 2.2) is the ratio of the driving force for phase separation and the resisting force (κ_0) against phase separation. Consequently, as D increases, so does the driving force for phase separation, and phase-separated structures with smaller droplet sizes result. The number density increases with D since, as mentioned previously, N_d is inversely proportional to $\langle d^*\rangle$. Lastly, there does not seem to be any correlation between $\langle S_f\rangle$ and D, since the formation of almost spherical droplets is characteristic to PDLCs formed by the PIPS method.

3.4. Voronoi Polygons and Random Droplet Positional Order. In this paper, the usual statistical analysis of the Voronoi polygon parameters characterizing the polygon shape and size such as the area, perimeter, and shape factor of each polygon will not be performed. Instead, a statistical study of the number of edges N_e was done, such that the positional order of the droplets can be analyzed.[36] Figure 8 shows the Dirichlet tessellations (first column) and frequency histograms of the number of edges in the Voronoi polygons (second column) for case I at the following dimensionless times: $t^* = 50.19 \times 10^{-5}$ (first row), $t^* = 50.43 \times 10^{-5}$ (second row), and $t^* = 51.27 \times 10^{-5}$ (third row). The Voronoi polygons are obtained using the centers of gravity of the droplets, which are represented by the dots that are not on any edge. The remaining dots denote the intersection of two edges. A visual inspection of the Voronoi polygons (first column) indicates that, at each time step, there is a distribution of N_e. This is shown in the corresponding frequency histograms (second column), where N_e ranges from 4 to 7. The average N_e for the three times in Figure 8 are as follows for increasing time: 5.31, 5.58, and 5.45. These values are close to the average value of 6 for large samples.[36] When the centers of gravity are positioned in a regular array, such as in a hexagon, there is no variation in the number of polygon edges. In other words, all polygons have the same number of edges. On the other hand, when the centers of gravity are positioned randomly, there is a variation. Therefore, since there is a variation of number of polygon edges, the centers of gravity are randomly positioned.[36] This means that the corresponding droplets are also randomly positioned in the matrix, as required in PDLCs for efficient light scattering.

4. Conclusions

This paper presents results from a numerical study of the PIPS phenomena. Moreover, the simulation results describe the formation of PDLCs by the PIPS method if the curing temperature is above the nematic–isotropic transition temperature.

The numerical results from this study replicate frequently reported experimental observations on the formation of PDLCs by the PIPS method. The experimental observations, characteristic of PDLCs formed by the PIPS method, are the formation and evolution of a droplet-type morphology with its corresponding time-resolved light scattering intensity profiles $I(s,t)$. The numerical equivalence of $I(s,t)$ is the circularly averaged structure factor $S(k,t)$. The phase-separated structure is consistent with experimental observations, since the initial average concentration is typical of the values used in experiments in the formation of PDLCs by the PIPS method. The time evolution of $S(k^*,t^*)$ indicates that phase separation is continuous during polymerization after the polymerization and phase separation lag times, which is in accordance with experimental results found in the literature on the formation of PDLCs by the PIPS method. This is supported by the time evolution of the maximum value of the structure factor $S(k_m^*,t^*)$, which exhibits an exponential growth during the early stage but then slows down and saturates in the intermediate stage of SD. In addition, the time evolution of $S(k^*,t^*)$ indicates that k_m^* increases during the early stage but generally decreases during the intermediate stage. The decrease during the intermediate stage is consistent with experimental observations in the formation of PDLCs by the PIPS method. On the other hand, the increase during the early stage has not yet been observed experimentally. A plausible reason for this undetection is that the phase separation dynamics is too fast to be captured and recorded at very early times. Therefore, the numerical results indicate that the polymerization process is important during the early stage, while the phase separation process is dominant during the intermediate stage of polymerization-induced SD.

The frequency histograms for the dimensionless equivalent diameter of the solvent-rich nearly circular regions d^* and the shape factor S_f show that the phase-separated structure gradually evolves from a structure with a wide distribution of droplet sizes and shapes to one containing predominately one droplet size and shape range. This is required for PDLCs to be efficient light scatterers. In addition, as observed in PDLCs formed by the PIPS method, the histograms for S_f also indicate that the droplets are not perfectly circular.

The dimensionless characteristic time $\tau = 1.005 \times t_t^*$, where t_t^* is the dimensionless transition time between the early and intermediate stages of SD, $\langle d^*(\tau)\rangle$, $\langle S_f(\tau)\rangle$, and $N_d(\tau)$ depend on the relative magnitudes of the dimensionless diffusion coefficient D and rate constant K_1. As D or K_1 increases, τ and $\langle d^*(\tau)\rangle$ decrease while $N_d(\tau)$ increases. The numerical results indicating that $\langle d^*(\tau)\rangle$ decreases as K_1 and $N_d(\tau)$ increase are consistent with experimental observations on the formation of PDLCs by the PIPS method.

Included in the morphological analysis is the determination of the positional order of the droplets. Using Dirichlet tessellations on the centers of gravity of the droplets, Voronoi polygons are obtained. Since there is a variation of the number of edges from droplet to droplet, it is concluded that the droplets are randomly positioned in the matrix. This is also a requirement for PDLCs to be efficient light scatterers.

In conclusion, as expected in SD the droplets are fairly uniform in size and shape and randomly distributed within the matrix. The results presented in this paper provide a better understanding of the parameters that affect the droplet size, shape, and position. This understanding and that presented in our previous paper on the droplet size selection mechanism allow for better control in PDLC film fabrication.

Acknowledgment. This work is supported by a grant from the Natural Sciences and Engineering Research Council of Canada (NSERC). The authors are grateful to CRAY Research (Canada) Inc. for a grant to defray the computational cost of this work and for technical assistance in using the CRAY C98/8256 supercomputer. P.K.C. acknowledges his postgraduate scholarships from the NSERC and the Fonds pour la Formation de Chercheurs et l'Aide à la Recherche du Québec (FCAR).

References and Notes

(1) Doane, J. W.; Vaz, N. A.; Wu, B.-G.; Zumer, S. *Appl. Phys. Lett.* **1986**, *48*, 269.
(2) Vaz, N. A.; Smith, G. W.; Montgomery, G. P. *Mol. Cryst. Liq. Cryst.* **1987**, *146*, 1.
(3) Lackner, A. M.; Margerum, J. D.; Ramos, E.; Lim, K.-C. *Proc. SPIE* **1989**, *1080*, 53.
(4) Drzaic, P. S. *Liquid Crystal Dispersions*; World Scientific: Singapore, 1995.
(5) Hirai, Y.; Niiyama, S.; Kumai, H.; Gunjima, T. *Proc. SPIE* **1990**, *1257*, 2.
(6) West, J. L. *Mol. Cryst. Liq. Cryst.* **1988**, *157*, 427.
(7) Kyu, T.; Mustafa, M.; Yang, J.-C.; Kim, J. Y.; Palffy-Muhoray, P. *Stud. Polym. Sci.* **1992**, *11*, 245.
(8) Kim, J. Y.; Palffy-Muhoray, P. *Mol. Cryst. Liq. Cryst.* **1991**, *203*, 93.
(9) Kim, J. Y.; Cho, C. H.; Palffy-Muhoray, P.; Mustafa, M.; Kyu, T. *Phys. Rev. Lett.* **1993**, *71*, 2232.
(10) Smith, G. W.; Vaz, N. A. *Liq. Cryst.* **1988**, *3*, 543.
(11) Gunton, J. D.; San Miguel, M.; Sahni, P. S. In *Phase Transitions and Critical Phenomena*; Domb, C., Lebowitz, J. L., Eds.; Academic Press: New York, 1983; Vol. 8.
(12) Chan, P. K.; Rey, A. D. *Comput. Mater. Sci.* **1995**, *3*, 377.
(13) Chan, P. K.; Rey, A. D. *Macromol. Theory Simul.* **1995**, *4*, 873.
(14) Jin, J.-M.; Parbhakar, K.; Dao, L. H. *Comput. Mater. Sci.* **1995**, *4*, 59.
(15) Lal, J.; Bansil, R. *Macromolecules* **1991**, *24*, 290.
(16) Bansil, R. *J. Phys. IV (Paris)* **1993**, *3*, 225.
(17) Kuwahara, N.; Kubota, K. *Phys. Rev. A* **1992**, *45*, 7385.
(18) Kubota, K.; Kuwahara, N. *Mod. Phys. Lett. B* **1992**, *6*, 1089.
(19) Chakrabarti, A.; Toral, R.; Gunton, J. D.; Muthukumar, M. *J. Chem. Phys.* **1990**, *92*, 6899.
(20) Brown, G.; Chakrabarti, A. *Phys. Rev. E* **1993**, *48*, 3705.
(21) Bates, F. S.; Wiltzius, P. *J. Chem. Phys.* **1989**, *91*, 3258.
(22) Hashimoto, T.; Itakura, M.; Hasegawa, H. *J. Chem. Phys.* **1986**, *85*, 6118.
(23) Vaz, N. A.; Smith, G. W.; Montgomery, G. P. *Mol. Cryst. Liq. Cryst.* **1987**, *146*, 17.
(24) Montgomery, G. P.; Smith, G. W.; Vaz, N. A. In *Liquid Crystalline and Mesomorphic Polymers*; Shibaev, V. P., Lam, L., Eds.; Springer-Verlag: New York, 1994.
(25) Doane, J. W.; Golemme, A.; West, J. L.; Whitehead, J. B.; Wu, B.-G. *Mol. Cryst. Liq. Cryst.* **1988**, *165*, 511.
(26) Drzaic, P. S. *Proc. SPIE* **1990**, *1257*, 29.
(27) Friedman, A. *Mathematics in Industrial Problems: Part 3*; Springer-Verlag: New York, 1990.
(28) Lin, J.-C.; Taylor, P. L. *Mol. Cryst. Liq. Cryst.* **1993**, *237*, 25.
(29) Yu, Y.-K.; Wang, X.-Y.; Taylor, P. L. *J. Chem. Phys.* **1996**, *104*, 2725.
(30) Jin, J.-M.; Parbhakar, K.; Dao, L. H. *Liq. Cryst.* **1995**, *19*, 791.
(31) Yamanaka, K.; Inoue, T. *J. Mater. Sci.* **1990**, *25*, 241.
(32) Chen, W.; Kobayashi, S.; Inoue, T.; Ohnaga, T.; Ougizawa, T. *Polymer* **1994**, *35*, 4015.
(33) Okada, M.; Fujimoto, K.; Nose, T. *Macromolecules* **1995**, *28*, 1795.
(34) Ohnaga, T.; Chen, W.; Inoue, T. *Polymer* **1994**, *35*, 3774.
(35) Chan, P. K.; Rey, A. D. *Macromolecules* **1996**, *29*, 8934−8941.
(36) Kurzydlowski, K. J.; Ralph, B. *The Quantitative Description of the Microstructure of Materials*; CRC Press: New York, 1995.
(37) Skripov, V. P.; Skripov, A. V. *Sov. Phys. Usp. (Engl. Transl.)* **1979**, *22*, 389.
(38) Novick-Cohen, A.; Segel, L. A. *Physica D* **1984**, *10*, 277.
(39) Flory, P. J. *Principles of Polymer Chemistry*; Cornell University Press: Ithaca, NY, 1953.
(40) Cowie, J. M. G. *Polymers: Chemistry and Physics of Modern Materials*, 2nd ed.; Chapman and Hall: New York, 1991.
(41) Cussler, E. L. *Diffusion: Mass Transfer in Fluid Systems*; Cambridge University Press: Cambridge, 1984.
(42) Sperling, L. H. *Introduction to Physical Polymer Science*, 2nd ed.; John Wiley and Sons: New York, 1992.
(43) de Gennes, P. G. *J. Chem. Phys.* **1980**, *72*, 4756.
(44) Debye, P. *J. Chem. Phys.* **1959**, *31*, 680.
(45) Rundman, K. B.; Hilliard, J. E. *Acta Metall.* **1967**, *15*, 1025.
(46) Barton, J. M. In *Advances in Polymer Science*; Dusek, K., Ed.; Springer-Verlag: New York, 1985; Vol. 72.
(47) Stockmayer, W. H. *J. Chem. Phys.* **1943**, *11*, 45.
(48) Binder, K.; Stauffer, D. In *Applications of the Monte Carlo Method in Statistical Physics*; Binder, K., Ed.; Springer-Verlag: New York, 1987.
(49) Elliott, C. M.; Songmu, Z. *Arch. Ration. Mech. Anal.* **1986**, *96*, 339.
(50) Fletcher, C. A. J. *Computational Galerkin Methods*; Springer-Verlag: New York, 1984.
(51) Carey, G. F.; Oden, J. T. *Finite Elements: A Second Course*; Prentice-Hall: Englewood Cliffs, NJ, 1983.
(52) Chung, T. J. *Finite Elements Analysis in Fluid Dynamics*; McGraw-Hill: New York, 1978.
(53) Finlayson, B. A. *Nonlinear Analysis in Chemical Engineering*; McGraw-Hill: New York, 1980.
(54) Lifshitz, I. M.; Slyozov, V. V. *J. Phys. Chem. Solids* **1961**, *19*, 35.

MA961078W